ENVIRONMENTAL RESEARCH
LETTERS

LETTER

A quantitative explanation for the large impacts of El Niño during its decaying stage

Xuanliang Ji[1,2], **Juan Feng**[2,*], **Jianping Li**[3,4], **Xingrong Chen**[1] and **Chunzai Wang**[5,6]

[1] Key Laboratory of Research on Marine Hazards Forecasting, National Marine Environmental Forecasting Center, Ministry of Natural Resources, Beijing, People's Republic of China
[2] State Key Laboratory of Remote Sensing Science, Faculty of Geographical Science, Beijing Normal University, Beijing, People's Republic of China
[3] Frontiers Science Center for Deep Ocean Multi-spheres and Earth System/Key Laboratory of Physical Oceanography/Academy of the Future Ocean, Ocean University of China, Qingdao, People's Republic of China
[4] Laoshan Laboratory, Qingdao, People's Republic of China
[5] State Key Laboratory of Tropical Oceanography, South China Sea Institute of Oceanology, Chinese Academy of Sciences, Guangzhou, People's Republic of China
[6] Global Ocean and Climate Research Center, South China Sea Institute of Oceanology, Chinese Academy of Sciences, Guangzhou, People's Republic of China
[*] Author to whom any correspondence should be addressed.

E-mail: fengjuan@bnu.edu.cn

Keywords: Hadley circulation, El Niño cycle, sea surface temperature, diabatic heating, asymmetric structure, equatorial quasi-symmetric structure

Supplementary material for this article is available online

OPEN ACCESS

RECEIVED
13 March 2024

REVISED
14 June 2024

ACCEPTED FOR PUBLICATION
3 July 2024

PUBLISHED
19 July 2024

Abstract

This study examines the comparative atmospheric circulation and tropical sea surface temperature (SST) relationships during the developing and decaying stages of El Niño from a meridional structure standpoint. Results indicate a transition in the variability of the first two modes of the Hadley circulation (HC) during these stages, with the first mode exhibiting a larger explained variance in the decaying stage. The regime change in HC variability corresponds to underlying anomalous SST distributions, as confirmed by sensitive experiments. Quantitative assessment reveals the HC-SST response amplitudes are approximately two times stronger during the decaying stage compared to the developing stage. Employing the Kuo–Eliassen (KE) equation, diabatic heating anomalies during the decaying stage explain the difference in air-sea response intensity between the two stages. Diabatic heating variations are identified as the primary contributor to amplification or reduction of air-sea response intensity during the respective El Niño stages, providing insights into the different air-sea processes throughout the El Niño lifespan.

1. Introduction

El Niño, identified as a naturally recurring phenomenon characterized by fluctuations in sea surface temperature (SST) within the central-eastern Pacific Ocean, is notably renowned for its significant interannual climate variability (Bjerknes 1969, Neelin *et al* 1998). These variations exhibit diverse amplitudes, temporal progressions, and spatial configurations (Capotondi *et al* 2015, Timmermann *et al* 2018, Chen *et al* 2022, Chen and Fang 2023, Fang *et al* 2024), consequently exerting an impact on global climate (Freitas *et al* 2016, Guo *et al* 2020, Yang and Huang 2021). Previous studies have highlighted pronounced climate effects of El Niño during its recession stage, such as excessive precipitation in East Asia during post-El Niño summers due to the anomalous western North Pacific anticyclone (Wang *et al* 2000, Song and Zhou 2015, Piao *et al* 2020, Chen and Li 2023, Gao and Li 2023), anomalous drought in northeastern South America, and flooding on the tropical west coast and southeastern South America through teleconnections (Cai *et al* 2020). Although studies have shown similar amplitudes of SST anomalies (SSTA) between the developing and decaying stages (Kim and Yu 2022), greater impact observed during the decaying stage compared to the developing stage remains quantitatively unexplained in prior research.

As El Niño develops, the eastward propagation of warm Kelvin waves associated with the westerly anomalies in the central-eastern Pacific, corresponding with further warmer SSTA in that Pacific. Thus, this results in the skewness of SSTA increasing eastward along the equator. Additionally, negative anomalies in Indian–Pacific warm pool (McCreary *et al* 2005, Cai *et al* 2011) through the wind–upwelling–SST feedback (Wang 2019) and tropical Atlantic regions (Ham *et al* 2021, Kim and Yu 2022) by atmospheric bridge (Liao and Wang 2021) have been detected, which is favorable for El Niño growth (Wang and Wang 2021). An eastward shift in the intense precipitation region in the tropical Pacific was observed because of the eastward displacement of the ascending branch of the Walker Cell (WC; Yun *et al* (2021)). Positive SSTA can trigger the Pacific-North American pattern (PNA) response, affecting climates in North America (Soulard *et al* 2019). As El Niño weakens, strengthening easterly anomalies generate cold Kelvin waves in the western Pacific, causing a gradual decrease in SST in the central-eastern Pacific and the emergence of negative anomalies (Weisberg and Wang 1997, Song *et al* 2022). This leads to a westward shift in the WC's ascending position (Timmermann *et al* 2018, Chen *et al* 2022), affecting East Asia climates differently. Additionally, a negative PNA teleconnection response is likely due to significant negative SSTA in the equatorial Pacific (Wang *et al* 2021). Moreover, in the decaying stage of El Niño events, SST in the peripheral regions of the equatorial central-eastern Pacific demonstrate disparate rates of decline. Specifically, negative anomalies are observed to the north of the equator, while positive anomalies are present to the south of the equator. (Stuecker *et al* 2015, Song *et al* 2022). Additionally, it is reported that the meridional distribution of SSTA exhibits different characteristics as El Niño develops or dissipates, displaying by quasi-symmetric or asymmetric feature (Feng *et al* 2023). Therefore, notable variations in tropical SSTA and the resulting climate impacts are evident during different El Niño stages.

The Hadley circulation (HC) plays a vital role in regulating global and regional climates. The primary mode of long-term variability of seasonal HC presents an equatorial asymmetric (EA) structure, and the second leading mode displays an equatorial symmetric (ES) pattern (Ma and Li 2008, Nguyen *et al* 2013, Sun and Zhou 2014). Previous studies have demonstrated that the SST meridional gradient significantly influence the strength and spatial distribution of HC (Lindzen and Nigam 1987, Numaguti 1995, Bordoni and Schneider 2010, Feng *et al* 2021, Yun *et al* 2021). Theoretical analyses suggest that the meridional gradient of radiative equilibrium temperature is crucial for determining HC strength by modifying boundary layer convergence and atmospheric thermal structures (Held and Hou 1980). Off-equatorial heating can trigger anomalous cross-equatorial HC patterns (Lindzen and Hou 1988). Numerical experiments have emphasized the sensitivity of lower atmospheric convergence and divergence to the meridional distribution of heating profile (Hou 1998, Fang and Tung 1999, Wang *et al* 2019). The primary modes of HC variability are significantly correlated with the corresponding meridional structure of SSTA (Xie *et al* 2022, Li *et al* 2023). Moreover, different stages of El Niño can result in varying structural anomalies within the HC (Guo and Tan 2018, Feng *et al* 2023). Thus, the noticeable spatial disparity in SST distribution during various El Niño stages leads to distinct effects on the HC (Feng *et al* 2023). However, can this phenomenon regulate the characteristics of HC variability? Additionally, the intricate link between SST and HC raises the question of whether spatial structural variations in SST during different stages can induce changes in the HC-SST relationship. These questions remain unanswered. Therefore, a quantitative analysis is conducted by examining the connection between SST and HC from the perspective of different meridional structures to explore the impact of various El Niño stages on the air-sea interaction as well as the relevant physical process. Specifically, section 2 covers the data and methods, section 3 explores HC variability and evaluates the linkage between SST and HC, section 4 discusses key physical processes, and Section 5 provides a conclusion.

2. Methods and data

2.1. Reanalyzes

This study utilizes six sets of atmospheric reanalysis data covering the period from 1980 to 2018 (table 1). The datasets are interpolated to a horizontal resolution of 2.5°× 2.5° to calculate the ensemble mean field. The analysis is based on the ensemble field to enhance the robustness of the findings. Monthly-mean outgoing longwave radiation (OLR) obtained from NOAA climate diagnostics center (CDC; Liebmann and Smith (1996)) and the monthly-mean precipitation from Global Precipitation Climatology Project version 2.3 (GPCP; Adler *et al* (2018)) are used to depict the convection process, both at a common horizontal resolution of 2.5°× 2.5°. Moreover, ERA5 daily data at 00:00 UTC, including atmospheric temperature, zonal and meridional wind speeds (u, v), and pressure velocity (ω, unit: Pa s^{-1}) is used to evaluate the dominant driving process influencing the predominant mode of HC variability. Two oceanic datasets, including NOAA extended reconstructed SST v5 (ERSST5; Huang *et al* 2017) and the Met Office Hadley Centre Sea Ice and SST data set (HadISST) (Rayner *et al* 2003), are also utilized to capture the variations in SSTA.

Table 1. List of the atmospheric reanalyzes for meridional wind used in this study.

Datasets	Abbreviation	References
Japanese 55 year Reanalysis	JRA55	Kobayashi *et al* (2015)
Modern-Era Retrospective analysis for Research and Applications v2	MERRA2	Gelaro *et al* (2017)
National Centers for Environmental Prediction National Center for Atmospheric Research (NCEP-NCAR) Reanalysis 1	NCEP1	Kalnay *et al* (1996)
NCEP-Department of Energy Reanalysis 2	NCEP2	Kanamitsu *et al* (2002)
European Center for Medium-Range Weather Forecasts (ECMWF) Era-Interim	ERAI	Dee *et al* (2011)
ECMWF Reanalysis v5	ERA5	Hersbach *et al* (2020)

2.2. Quantitative methods

This study employed the mass stream function (MSF, S1 Methods) to quantify the mean meridional circulation. To quantitatively evaluate the intensity of air-sea interaction, we decompose the HC and SST into their symmetric (HC-ES, SST-ES) and asymmetric (HC-EA, SST-EA) components according to Feng *et al* (2016) (S2 Methods). Subsequently, we derive the first principal component (PC1) values for each component using an empirical orthogonal function (EOF) decomposition. Thus, the quantitative measure of climate response strength is defined as follows:

$$\text{Ratio} = \frac{\text{Reg}\left[\text{PC1}\left(\text{SST}-\text{EA}\right), \text{PC1}\left(\text{HC}-\text{EA}\right)\right]}{\text{Reg}\left[\text{PC1}\left(\text{SST}-\text{ES}\right), \text{PC1}\left(\text{HC}-\text{ES}\right)\right]}, \tag{1}$$

where PC1 (SST-ES) is the PC1 of the first mode of SST-ES variability, and the other variables remain the same. The denominator (numerator) represents the regression ratio of HC-ES (HC-EA) to SST-ES (SST-EA). This *Ratio* serves as an indicator of the intensity of the relationship between different meridional structures of tropical SST and atmospheric circulation (Feng *et al* 2016). A higher ratio value signifies a heightened sensitivity to the spatial distribution of SST, suggesting a more robust tropical air-sea interaction.

2.3. Extended Kuo–Eliassen equation

To isolate and quantify the physical terms such as diabatic heating, friction, and the fluxes of eddy heat and momentum that affect the HC response (Hoskins *et al* 2020, Hoskins and Yang 2021, Hill *et al* 2022), we employ the extended Kuo–Eliassen (KE) equation (Kim and Lee 2001, Chemke and Polvani 2021, Chemke 2022, Zaplotnik *et al* 2022) to solve for the zonal-mean meridional streamfunction (ψ^{KE}). The extended KE equation, formulated without a quasi-geostrophic assumption, is an elliptic second-order partial differential equation and is represented as follows:

$$\begin{aligned}
&f^2\frac{g}{2\pi R\cos\phi}\frac{\partial^2\psi^{\mathrm{KE}}}{\partial P^2}+\frac{g}{2\pi R}\frac{\partial}{R\partial\phi}\left(\frac{1}{R\cos\phi}\frac{\partial}{\partial\phi}S^2\right)\\
&\quad+\frac{g}{2\pi R}\frac{R_d}{P}\frac{\partial}{R\partial\phi}\left(\frac{\partial[T]}{R\cos\phi\partial\phi}\frac{\partial\psi^{\mathrm{KE}}}{\partial P}\right)\\
&\quad+f^2\frac{g}{2\pi R\cos\phi}\left(\frac{\partial[u]}{\partial P}\frac{\partial^2\psi^{\mathrm{KE}}}{R\partial\phi\partial P}+\frac{\partial^2[u]}{\partial P^2}\frac{\partial\psi^{\mathrm{KE}}}{R\partial\phi}\right.\\
&\quad\left.-\frac{\partial^2([u]\cos\phi)}{R\cos\phi\partial\phi\partial P^2}\frac{\partial\psi^{\mathrm{KE}}}{\partial P}-\frac{\partial([u]\cos\phi)}{R\cos\phi\partial}\frac{\partial^2\psi^{\mathrm{KE}}}{\partial P^2}\right)\\
&=\frac{R_d}{P}\frac{\partial[J]}{R\partial\phi}-\frac{R_d}{P}\frac{\partial}{R\partial\phi}\frac{\partial([u'T']\cos\phi)}{R\cos\phi\partial\phi}-f\frac{\partial[F_\lambda]}{\partial P}\\
&\quad+f\frac{\partial^2\left([u'v]\cos^2\phi\right)}{R\cos^2\phi\partial P\partial\phi}+f\frac{\partial^2[u'\omega']}{\partial P^2}-\frac{1}{\rho[\theta]}\frac{\partial}{R\partial\phi}\frac{\partial[\omega'\theta']}{\partial P},
\end{aligned} \tag{2}$$

where, f is Coriolis parameter, R is earth's radius (6,371,000 m), g is gravity (9.81 m·s^{-2}), ϕ is latitude, P is pressure (Pa), R_d is the gas constant of dry air (287 J·kg^{-1} K^{-1}), ρ is air density, square bracket and prime represent the zonal-mean and monthly-mean parts, and deviation from zonal-mean and monthly mean, respectively. S^2 is the static stability. J, T, u, v, ω, F_λ and θ are the diabatic heating, atmospheric temperature, zonal wind, meridional wind, pressure velocity, friction, and potential temperature, respectively. $[v'T']$, $[u'v']$, $[u'\omega']$ and $[\omega'\theta']$ are the eddy heat flux, eddy momentum flux, vertical eddy momentum flux and vertical eddy heat flux, respectively.

2.4. Model

The atmospheric general circulation model employed here is the National Center for Atmospheric Research (NCAR) Community Atmospheric Model, version 5 (CAM5). The CAM5 serves as a comprehensive global climate model and constitutes the atmospheric component within the NCAR Community Earth System Model (CESM). With a horizontal resolution measuring 1.9° × 2.5° and consisting of 30 vertical layers, CAM5 possesses the capacity to accurately replicate various climatic characteristics (Zhou *et al* 2020).

2.5. Statistical method

An El Niño event occurs when the three-month running mean Niño 3.4 index (areal-averaged SSTA in

170°–120°W, 5°S–5°N) exceeds 0.5 °C for 5 consecutive months or longer. Finally, ten events are selected: 1982/1983, 1986/1988, 1991/1992, 1994/1995, 1997/1998, 2002/2003, 2004/2005, 2006/2007, 2009/2010, and 2015/2016. The former ten years are designated as El Niño developing years, and the latter ten years are classified as El Niño decaying years. In our analysis, we considered entire years for both developing and decaying stages. To investigate HC and SST variability, we employ various methods including EOF analysis, the North test, student's two-sided test, correlation (r), and linear regression.

3. Results

3.1. Regime shift of HC variability during the two stages

Initially, an analysis is conducted on HC variability features during El Niño cycle (figure 1). The HC-EOF1 in developing stage (figure 1(a)) exhibits significant ES features with an explained variance of 26.92%, consistent with the HC-EOF2 for the long-term HC variability, primarily influenced by El Niño (Zhou and Wang 2006, Ma and Li 2008, Sun *et al* 2019). The HC-EOF2 (figure 1(b)) shows EA features, aligning with the HC-EOF1 mode in the long-term HC variability (Dima and Wallace 2003). However, in decaying stage, the first mode becomes dominated by an EA with ∼40% explained variance, corresponding to the HC-EOF2 in developing stage but with a stronger intensity. The second mode becomes ES with a decreasing explained variance of nearly 16.99%, which is less than that of HC-EOF1 during developing stage. This indicates that a regime replacement of the dominant mode occurs during different stages, which further suggests disparities in the air-sea response.

3.2. Varying extents of the HC-SST response during the two stages

Subsequently, a quantitative evaluation of tropical air-sea interactions as El Niño transitions is conducted using equation (2). Figure 2 depicts the relationship between HC-ES (HC-EA) PC1 and SST-ES (SST-EA) PC1, as well as their response ratio during the two stages. Based on the ensemble filed the ratio of HC-EA to SST-EA is approximately 2.39 times (figure 2(b)) than that of HC-ES to SST-ES during developing stage, which is significantly lower than the ratio value of 5.98 times (figure 2(d)) during the decaying stage. Moreover, the response amplitude of HC-EA to SST-EA during decaying stage (figure 2(c), dark-cyan) is much larger than that during developing stage (figure 2(a), dark-cyan). This observation implies that the HC-EA component is intensified considerably during decaying stage (figures S1(a) vs (c)). Meanwhile, the response of the HC-ES to SST-ES does not exhibit significant variations in two stages (figures 2(a) and (c), deep-pink), which could be further examined from the minimal changes in the HC-ES intensity (figures S1(b) vs (d)). Similar results have also been detected between HadISST and atmospheric datasets (figure S2). This indicates that, under equivalent SSTA forcing intensity, the variations in HC-EA component are more suppressed (pronounced) during developing (decaying) stage, leading to a decreased (increased) explained variance in EA mode. This suggests that tropical air-sea interactions are more intense during decaying stage, providing a measurable explanation for the greater impact of decaying stage on climate dynamics compared to developing stage. Therefore, what changes in the fundamental thermal conditions have caused the distinct extent of tropical air-sea interaction?

4. Discussion

To explore the controlling mechanisms behind the varied responses as stage transitions, we examine the changes in meridional distributions of zonal-mean zonal wind, OLR, and precipitation (figure 3). During developing stage, persistent westerlies transport warm water from the western to eastern Pacific (Jin 1997, Wang *et al* 2023), leading to a significant rise in positive SSTA in the tropical Pacific (Timmermann *et al* 2018, Hayashi *et al* 2020). An ES feature manifests in the zonal-mean zonal wind (figure 3(a), red line), resulting in corresponding characteristics in zonal-mean SSTA (Feng *et al* 2023). Moreover, an intensified deep convection moves eastward because of the eastward displacement of WC (figure S3(a)). The zonal-mean OLR shows an ES pattern (figure 3(a), green line), showing an inverse correlation with meridional SSTA distribution. Increasing SST leads to decreasing OLR, culminating in deep convection initiation near the equator (Kohyama and Tozuka 2016, Chaudhari *et al* 2017), signifying intense convection in the equatorial area (Freitas *et al* 2016). The strong correlation between OLR and precipitation suggests that enhanced deep convection causes localized heavy rainfall events (Xu 2013, Harrison and Chiodi 2015). As SSTA in the equatorial central-eastern Pacific region increase, intense convection moves eastward, indicating a zonal shift in oceanic latent heat release. This leads to a zonal shift in the center of intense precipitation anomalies (figure S4(a)), displaying a quasi-symmetric pattern in the meridional direction (figure 3(a), blue line).

With the phase transition, there is a noticeable and asymmetric decline in the westerlies on either side of equator in tropical Pacific Ocean (Song *et al* 2019, Chen and Li 2021), displaying an EA pattern (figure 3(b), red line). The SST maintains significant positive anomalies to the south and rapidly transitions to negative anomalies to the north (Stuecker

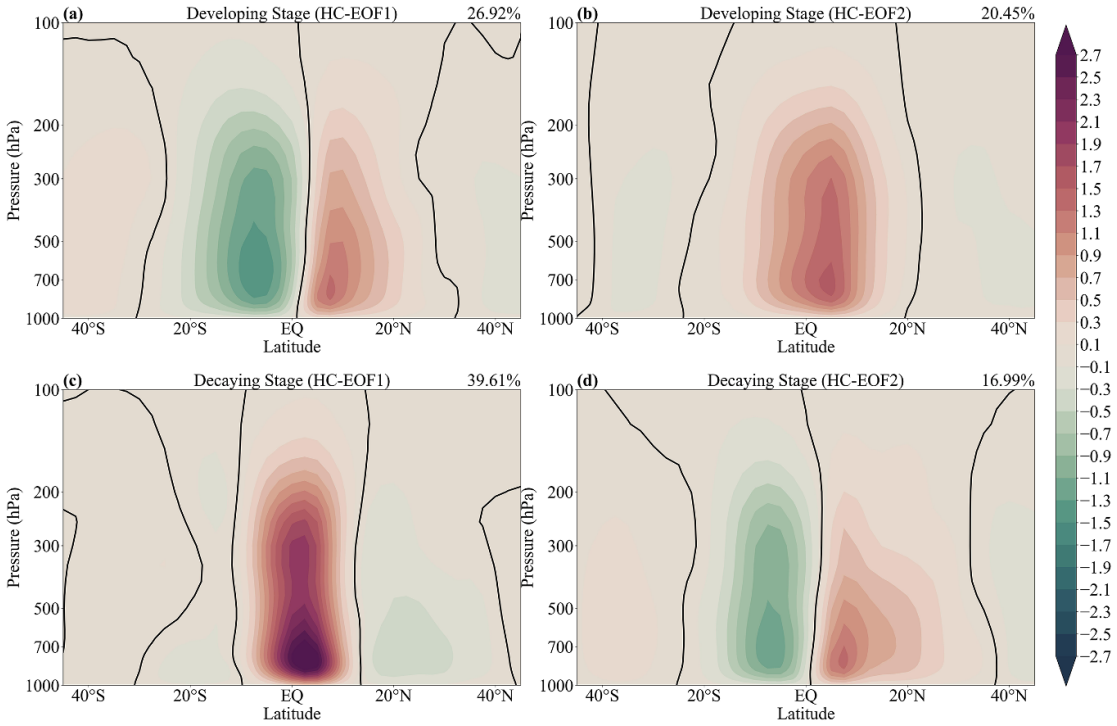

Figure 1. Spatial distribution features of the HC-EOF1 and HC-EOF2 during the El Niño developing and decaying stages. (a) HC-EOF1 during the El Niño developing stage under the ensemble mean field (with an interval of 0.2×10^{10} kg s^{-1}). The zero line is thick. (b) Same as in (a), but for the HC-EOF2. (c) and (d) Same as in (a) and (b), but for the HC EOF1 and EOF2 during the El Niño decaying stage. The sample for EOF analysis is 120.

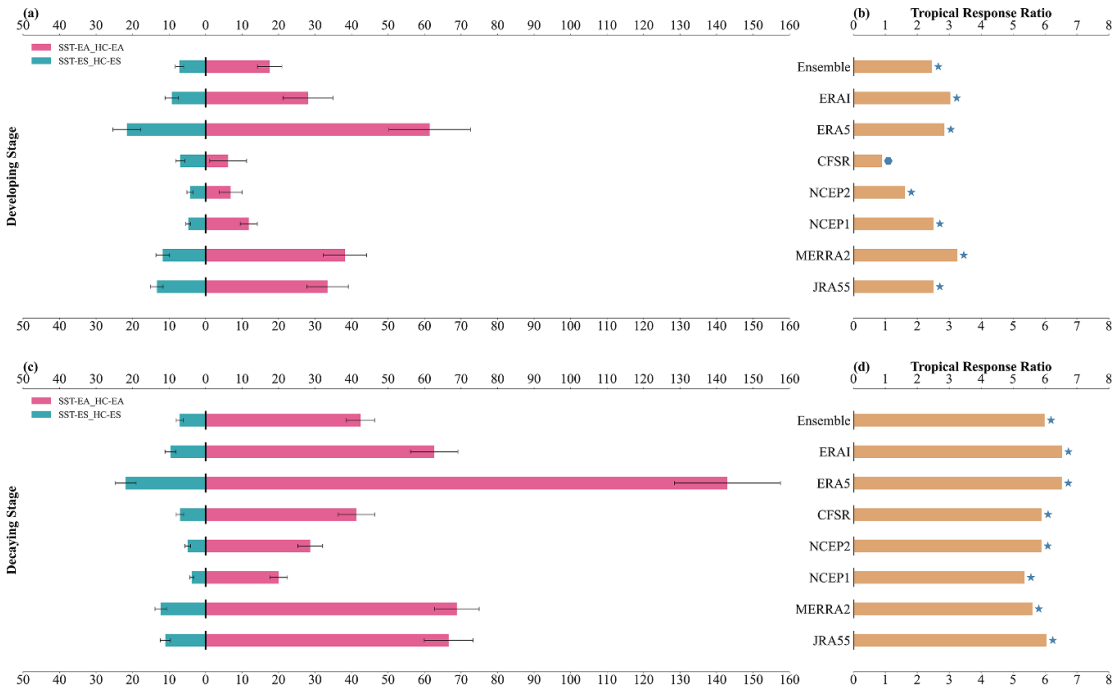

Figure 2. Response of the HC to SST during the developing and decaying stages based on ERSST5 and the atmospheric reanalyzes. (a) The regression coefficients of HC to SST during the developing stage (SST-EA PC1 to HC-EA PC1 is in dark-cyan, and SST-ES PC1 to HC-ES PC1 is in deep-pink. (b) The extent of tropical air-sea interaction. (c) and (d) Same as in (a) and (b), but for the results during the decaying stage. The blue star represents that the trend of HC-EA/SST-EA is significantly greater than that of HC-ES/SST-ES at the 90% confidence level (based on the running slope difference (RSD) *t* test, S3 Methods). The hexagon denotes that trend of HC-ES/SST-ES is significantly greater than that of HC-EA/SST-EA at the 90% confidence level (based on the RSD *t* test).

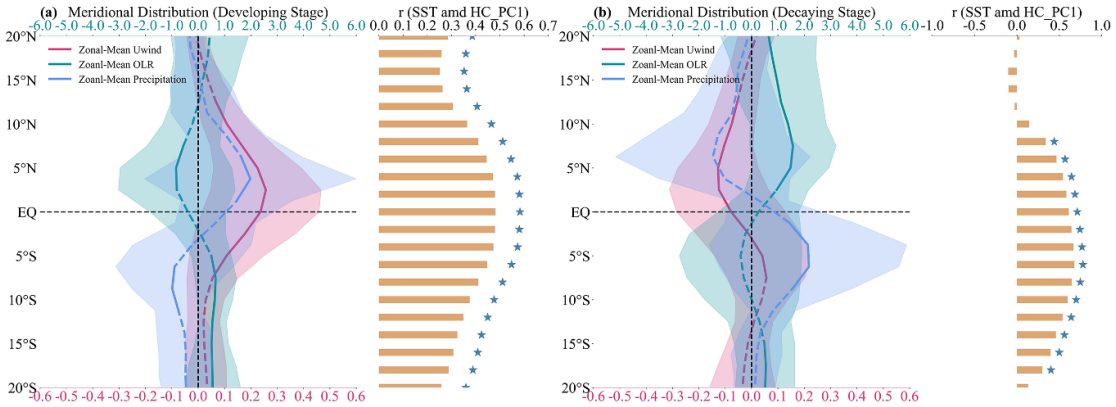

Figure 3. Meridional distribution of zonal-mean zonal wind (unit: m s^{-1}, values multiplied by 4), OLR anomaly (unit: W m^{-2}), precipitation anomaly (unit: mm d^{-1}, values multiplied by 10), and the correlation coefficients between HC-PC1 and zonal-mean SSTA based on ERSST5 during the developing (a) and decaying (b) stage. The shading for each variable is referenced to its one standard deviation. The star represents represent significance at the 0.05 level using the student's two-sided test.

et al 2015, Song *et al* 2022), resulting in an asymmetric zonal-mean SSTA structure. Asymmetric heating near the equator causes the center of negative OLR anomaly in tropical Pacific to shift towards the southern region (figure S3(b)), accompanied by a pronounced precipitation center in the same vicinity (figure S4(b)). The meridional distributions of OLR and precipitation anomalies exhibit an EA pattern (figure 3(b)). As noted, low-level atmospheric circulation is sensitive to the meridional structure of SSTA changes (Lindzen and Nigam 1987). Thus, in this stage, a slight deviation of a few degrees from the equator in SSTA induces anomalous latent release and enhance the deep convection south of the equator, which further results in the asymmetric feature of the HC (figure 1(c)). Moreover, the zonal-mean SST, OLR, and precipitation demonstrate coherent temporal and latitudinal changes, coinciding with the migration of the extreme center from north to south as the El Niño event progresses (figure S5). This further indicates the impact of underlying heating source changes on atmospheric convection activity.

Additionally, comparing the correlation between the HC-PC1 and zonal-mean SSTA during the two stages (figures 3(a) and (b), right panel) reveals distinct patterns. During developing stage, the correlation values exhibit an ES distribution, peaking around the equator ($r = 0.48$, $p < 0.05$). Conversely, the decaying stage shows an EA feature, peaking between 5° and 10°S ($r = 0.68$, $p < 0.05$). Similar results have also been detected between HadISST and HC-PC1 (figure S6). Therefore, both spatial configurations align with the distribution of HC-EOF1 mode in each stage. This alignment suggests that shifts in meridional location of tropical heating source can induce anomalous perturbations in tropical meridional circulation (Gill 2007, Feng *et al* 2016). Therefore, the meridional positioning of the underlying heat source plays a pivotal role in HC variability by modulating the amplitude of the tropical air-sea response during El Niño cycle (figure 2). Next, the influence of meridional distribution changes in SSTA on HC is further assessed based on numerical simulation.

We conduct experiments using CAM5 to validate our hypothesis. Three experiments are conducted: the first is a free-run experiment using the climatological SST field as the baseline. The second and third sets involves incorporating monthly SST anomalies during developing and decaying stages, respectively, into the corresponding months of the climatological SST field. Each experimental group consists of 30 years of numerical simulations. Ensemble averaging is performed on results from the 2nd to the 30th year for each experiment set to obtain the climatological distribution of HC and spatial anomalies of HC during developing and decaying stages (figure 4). The simulated climatological HC closely matches the reanalysis results (Hur *et al* 2021), exhibiting a high spatial correlation of 0.99 and showcasing the model's ability to replicate HC features. Adding SST anomalies during developing stage leads to an anomalous HC-ES pattern (figure 4(a)), consistent with observations. Nonetheless, discrepancies in the meridional circulation over tropical Northern Hemisphere region compared to observations may be attributed to limited feedback mechanisms between the atmosphere and ocean (Jin 1997), and the influence of Northern Hemisphere landmasses on the air-sea interaction dynamics (Liu *et al* 2020). This discrepancy suggests the presence of significant air-sea interactions cannot be adequately represented by a basic atmospheric circulation model driven solely by ocean temperatures. Conversely, exposure to SST anomalies during the decaying stage results in an asymmetric configuration (figure 4(b)), with a rising branch near 10°S and a sinking branch near 20°N, further supporting the hypothesis that distinct meridional SST structures

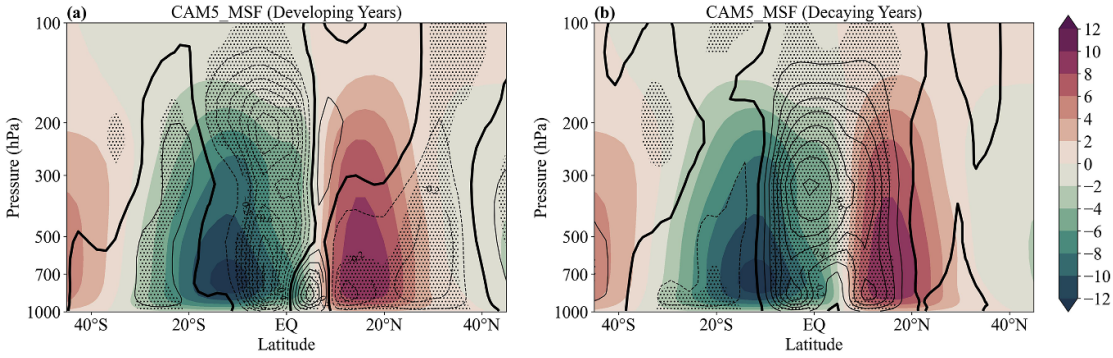

Figure 4. Spatial distribution of climatological MSF, and its anomalies from CAM5 model during El Niño developing and decaying stages. (a). The MSF anomalies during El Niño developing stage (contour line, with an interval of 0.2×10^{10} kg s^{-1}) and its climatological mean (shading). (b) As in (a), but for El Niño decaying stage. Solid (dotted) contour line is positive (negative), and the zero line is thickened. The dark spot represent significance at the 0.05 level using the student's two-sided test.

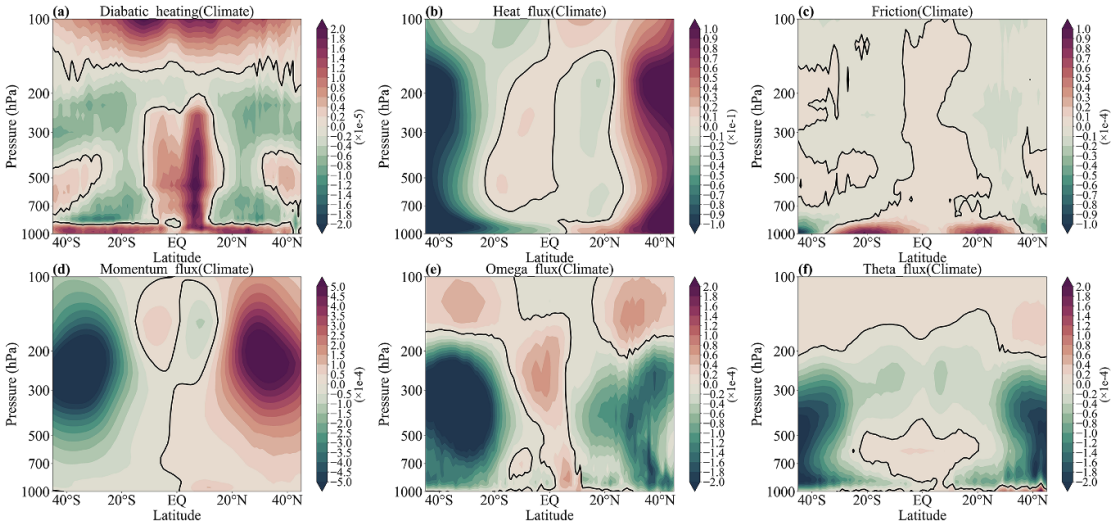

Figure 5. Climatological distribution of the six terms in the right hand of equation (2) for the ψ^{KE} without exact solution over the entire period. (a) Diabatic heating (with an interval of 0.2×10^{-5} K s^{-1}), (b) eddy heat flux (with an interval of 0.1×10^{-1} K*m*s^{-1}), (c) friction (with an interval of 0.1×10^{-4} m s^{-2}), (d) eddy momentum flux (with an interval of 0.5×10^{-4} m^2 s^{-2}), (e) vertical momentum flux (with an interval of 0.2×10^{-4} Pa m s^{-2}) and (f) vertical heat flux (with an interval of 0.2×10^{-4} K Pa s^{-1}). The black thickened line is zero line for the six terms.

significantly influence HC variability during these two stages.

Although the significance of changes in SSTA meridional structures is acknowledged, the physical process of how anomalous warming impacts the HC remains unclear. Thus, we employ the extended KE equation to understand the relevant quantitative contributions. The ψ^{KE} derived from equation (2) demonstrates a high degree of agreement with MSF (figure S7). Additionally, the magnitude of diabatic heating (figure S8(a)) is comparable to that of ψ^{KE}, suggesting that diabatic heating term is a primary contributor to the MSF. The pattern correlations between ψ^{KE} and the six terms are presented in table 2. The diabatic heating is the dominant driver of climatological HC ($r = 0.85$, $p < 0.05$). This is mainly attributed to diabatic heating's modulation of tropical latent heat release (Chemke and Polvani 2019) and subtropical cooling processes (figure 5(a)) (Zaplotnik *et al* 2022), which correspond to the ascending and downdraft branches of HC, respectively.

Furthermore, it is evident that friction is positively correlated with climatological ψ^{KE} ($r = 0.84$, $p < 0.05$). The frictional force acting on the zonal wind can be considered to approximately balance the Coriolis force acting on the meridional wind ($f\psi \propto -F_x\overline{u_{sfc}}$ in Chemke and Yuval (2023)). Therefore, frictional force primarily controls the horizontal motion of the lower part of HC (figure 5(c)). Extratropical eddy heat and momentum fluxes are generally considered to influence the dynamics in mid-latitude region, thus affecting the boundaries and width of the HC (Zurita-Gotor 2019). Therefore, the divergence of subtropical momentum (figure 5(d)) and heat fluxes (figure 5(b)) induced by tropical eddies is also an important driver of HC variability ($r = 0.82$

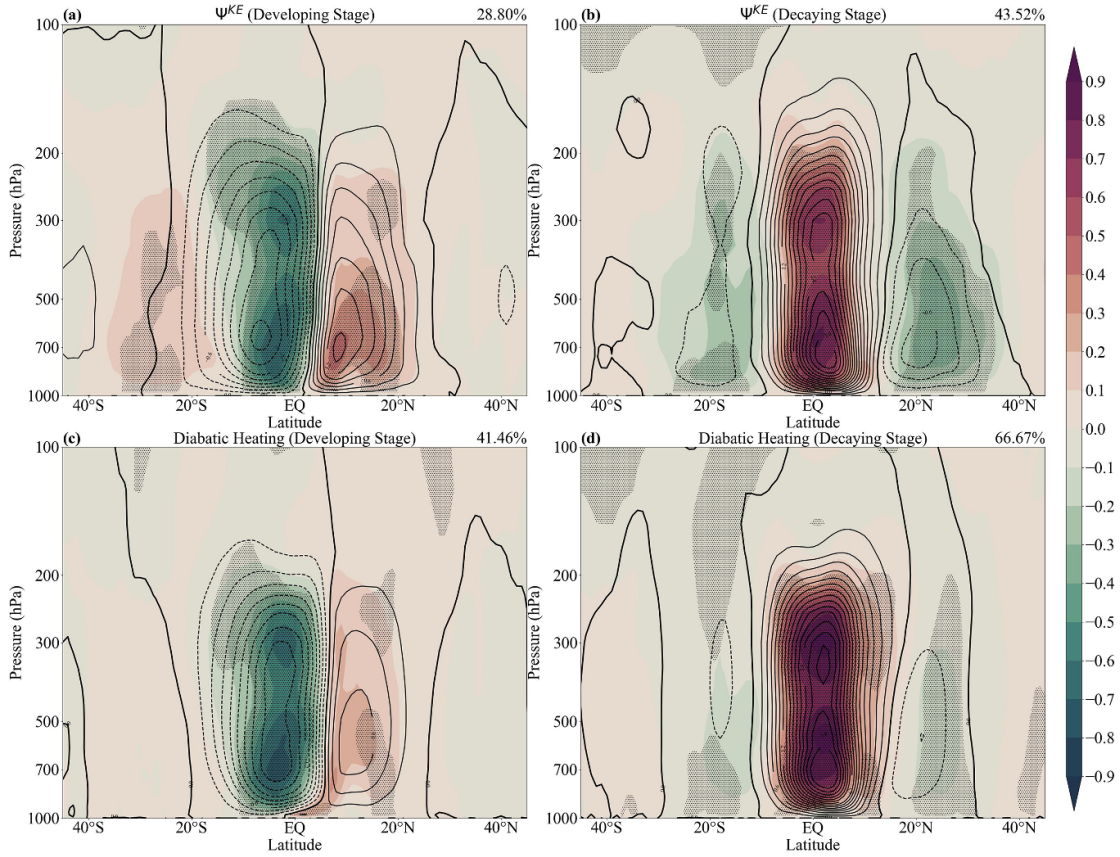

Figure 6. Spatial anomalous distribution of ψ^{KE}, diabatic heating and their EOF1 modes during El Niño developing and decaying stages. (a) The ψ^{KE} anomalies during El Niño developing stage (shading, with an interval of 0.1×10^{10} kg s^{-1}), and the EOF1 mode of ψ^{KE} variability during El Niño developing stage (contour line, with an interval of 0.2×10^{10} kg s^{-1}). (b) As in (a), but for the results during decaying stage. (c) and (d) The same as in (a) and (b), but for the results of diabatic heating term. Solid (dotted) contour line is positive (negative), and the zero line is thickened.

and 0.83, respectively, $p < 0.05$). Moreover, the vertical eddy momentum flux and vertical eddy heat flux exhibit negative correlations with HC ($r = -0.38$ and -0.46, respectively, $p < 0.05$), indicating that they weaken the tropical meridional circulation (figures S8(e) and (f)).

The anomalous distribution of HC represented by ψ^{KE} exhibits ES features in the developing stage (figure 6(a)) and EA features during the decaying stage (figure 6(b)). Additionally, the anomalous distributions of six terms demonstrate that the diabatic heating anomaly (figures 6(c) and (d)) is comparable in magnitude to ψ^{KE} anomaly, whereas the remaining five terms (figure S9) are generally an order of magnitude smaller. Furthermore, it is seen that the amplitude of diabatic heating anomalies during the decaying stage is roughly twice that of the developing stage (figures 6(c) vs (d)), comparable to the response ratio in ERA5 (figures 2(b) vs (d)). Furthermore, the spatial correlation coefficients between diabatic heating anomalies and ψ^{KE} anomalies remain strongly positive in both stages (table 2), confirming the dominant role of diabatic heating anomalies in influencing HC variability. The contributions of the other five terms in both phases are deemed negligible. Moreover, the EOF1 mode of ψ^{KE} anomalies during the two stages exhibits substantial agreement with that of diabatic heating (figure 6). This further suggests that the primary driver of different connection between HC and SST along the El Niño lifespan is the diabatic heating process.

Table 2. Spatial correlations between the ψ^{KE} and the relative contributing physical process during the climate state and two stages of El Niño. Only correlations exceeding the 0.05 significance threshold are shown.

	Climate state	Developing stage	Decaying stage
J	0.85	0.92	0.88
$V'T'$	0.83	0.26	0.24
Friction	0.84	0.36	0.35
$u'v'$	0.82	0.32	0.24
$u'w'$	−0.38	/	−0.11
$w'\theta'$	−0.46	−0.07	−0.14

Therefore, the relocation of the heating source, combined with increased deep convection and heating in the tropical troposphere, primarily controls the distribution of atmospheric perturbation potential energy (Stechmann and Ogrosky 2014, Zhang *et al* 2016, Dong *et al* 2017). Consequently, this process, driven by diabatic heating, significantly impacts HC variability, leading to diverse air-sea responses during El Niño transitions.

5. Conclusion

This study examines the key factors influencing HC-SST responses along El Niño lifespan. The analysis reveals a transition in HC variability, with HC-EOF1 exhibiting an ES (EA) feature during developing (decaying) stage. The response amplitude of HC to tropical SST is approximately doubled during decaying stage compared to developing stage, primarily driven by the anomalous SST structures during each stage. Sensitivity experiments confirm that the thermal state of the El Niño cycle significantly influences tropical air-sea interactions. By decomposing the streamfunction using the extended KE equation, we identify six key components, with diabatic heating playing a crucial role. It reveals that the magnitude of the MSF intensity change caused by the diabatic heating term during the decaying stage is twice that of the developing stage. Therefore, we ascertain that it is mainly due to the diabatic heating process contributing to the amplified air-sea response during the decaying stage. The influence of diverse El Niño stages on air-sea processes can be explained by the following steps:

(1) During the developing stage, the zonal-mean SSTA shows an ES distribution, which leads to a strengthened diabatic heating in the equatorial region (figures 6 and S10), and further result in an increasing low-level convergence activity, with deeper convection (negative OLR anomaly, figure S3) and heavier precipitation (figure S4) over tropical central-western Pacific Ocean regions. Thus, an ES structure of these dominant atmospheric processes (figure 3(a)) is generated, which strengthens the ES component of HC, paralleling to the primary HC ES mode during the developing stage.
(2) With the recession of El Niño, the asymmetric decay rate of westerlies on the flanks of equatorial Pacific Ocean (figure 3(b)), leads to a slower decline rate in SST south of the equator than north of the equator. The zonal-mean SSTA presents an EA structure, with a warmer heating locating around 5°–10°S. This indicates that more latent heat release occurs here. Further, it leads to a strengthened diabatic heating (figures 6 and S11) and causes an increasing low-level convergence activity (figures S3 and S4) over this region. Subsequently, the EA component of HC is strengthened, paralleling the dominant EA mode during this stage. Additionally, the larger anomaly amplitude of diabatic heating also leads to a greater intensity of tropical air-sea interaction in the recession stage.

Therefore, our study provides a quantitative explanation for the heightened climatic impact of El Niño during its decaying stage relative to its developing stage (Liu *et al* 2021, Yu *et al* 2022, Chen and Li 2023, Gao and Li 2023), with a specific perspective on the role played by the meridional distribution of SSTA in shaping the variability of HC by regulating the atmospheric diabatic heating process.

Data availability statement

The data atmosphere used in the manuscript are publicly available for NCEP1 and NCEP2 (https://psl.noaa.gov/data/gridded/), CFSR (https://rda.ucar.edu/datasets/), ERAI (https://apps.ecmwf.int/datasets/data/interim-full-mnth/levtype=pl/), ERA5 (www.ecmwf.int/en/forecasts/dataset/ecmwf-reanalysis-v5), JRA55 (https://rda.ucar.edu/data–sets/ds628.1/dataaccess/), MERRA2 (https://disc.–gsfc.nasa.gov/datasets?project=MERRA-2), NOAA-CDC-OLR (https://psl.noaa.gov/thredds/catalog/Datasets/interp_OLR/catalog.html), and NCAR-GPCP (https://climatedataguide.ucar.edu/climate-data/gpcp-monthly-global-precipitation-climatology-project). The SST data is publicly available for ERSST5 (www.esrl.noaa.gov/psd/data/gridded/) and for HadISST (https://climatedataguide.ucar.edu/climate-data/sst-data-hadisst-v11). The index for the El Niño stage definition is publicly available at https://origin.cpc.ncep.noaa.gov/products/analysis_monitoring/ensostuff/ONI_v5.php. A full description of CAM5 is available online at https://ncar.github.io/CAM/doc/build/html/cam5_scientific_guide/.

The data that support the findings of this study are openly available at the following URL/DOI: www.esrl.noaa.gov/psd/data/gridded/; https://climatedataguide.ucar.edu/climate-data/gpcp-monthly-global-precipitation-climatology-project; https://psl.noaa.gov/thredds/catalog/Datasets/interp_OLR/catalog.html; https://disc.gsfc.nasa.gov/datasets?project=MERRA-2; https://psl.noaa.gov/data/gridded/; https://rda.ucar.edu/datasets/; https://apps.ecmwf.int/datasets/data/interim-full-mnth/levtype=pl/; www.ecmwf.int/en/forecasts/dataset/ecmwf-reanalysis-v5; https://rda.ucar.edu/datasets/ds628.1/dataaccess/.

Acknowledgments

This work was supported by the National Key R&D Program of China (2023YFC3107702, 2022YFC3105102), the National Natural Science Foundation of China (42222501), the Project of Southern Marine Science and Engineering Guangdong Laboratory (Zhuhai) under Contract No. SML2023SP219, the State Key Laboratory of Tropical Oceanography, South China Sea Institute of Oceanology, Chinese Academy of Sciences (No. LTO2310), and the National Key Scientific and Technological Infrastructure project“Earth System

Numerical Simulation Facility" (EarthLab). We thank ŽIGA ZAPLOTNIK for sharing the extended KE equation solver program (https://doi.org/10.5281/zenodo.6349274).

Conflict of interest

The authors declare no conflicting interests.

ORCID iDs

Xuanliang Ji https://orcid.org/0000-0002-0718-7504
Juan Feng https://orcid.org/0000-0002-2382-8500
Jianping Li https://orcid.org/0000-0003-0625-1575
Xingrong Chen https://orcid.org/0000-0003-4748-3583

References

Adler R *et al* 2018 The global precipitation climatology project (GPCP) monthly analysis (new version 2.3) and a review of 2017 global precipitation *Atmosphere* **9** 138
Bjerknes J 1969 Atmospheric teleconnections from the Equatorial Pacific *Mon. Weather Rev.* **97** 163–72
Bordoni S and Schneider T 2010 Regime transitions of steady and time-dependent hadley circulations: comparison of axisymmetric and eddy-permitting simulations *J. Atmos. Sci.* **67** 1643–54
Cai W *et al* 2020 Climate impacts of the El Niño–Southern oscillation on South America *Nat. Rev. Earth Environ.* **1** 215–31
Cai W, van Rensch P, Cowan T and Hendon H H 2011 Teleconnection pathways of ENSO and the IOD and the mechanisms for impacts on Australian rainfall *J. Clim.* **24** 3910–23
Capotondi A *et al* 2015 Understanding ENSO diversity *Bull. Am. Meteorol. Soc.* **96** 921–38
Chaudhari H S, Hazra A, Pokhrel S, Chakrabarty C, Saha S K and Sreenivas P 2017 SST and OLR relationship during Indian summer monsoon: a coupled climate modelling perspective *Meteorol. Atmos. Phys.* **130** 211–25
Chemke R 2022 Large hemispheric differences in the Hadley cell strength variability due to ocean coupling *npj Clim. Atmos. Sci.* **5** 1
Chemke R and Polvani L M 2019 Opposite tropical circulation trends in climate models and in reanalyses *Nat. Geosci.* **12** 528–32
Chemke R and Polvani L M 2021 Elucidating the mechanisms responsible for hadley cell weakening under 4 × CO_2 forcing *Geophys. Res. Lett.* **48** e2020GL090348
Chemke R and Yuval J 2023 Human-induced weakening of the Northern Hemisphere tropical circulation *Nature* **617** 529–32
Chen L and Li G 2023 Asymmetric effect of ENSO in the decaying stage on the central China July precipitation *Clim. Dyn.* **61** 3029–45
Chen M C and Li T 2021 ENSO evolution asymmetry: EP versus CP El Niño *Clim. Dyn.* **56** 3569–79
Chen N and Fang X 2023 A simple multiscale intermediate coupled stochastic model for El Niño diversity and complexity *J. Adv. Modeling Earth Syst.* **15** e2022MS003469
Chen N, Fang X and Yu J-Y 2022 A multiscale model for El Niño complexity *npj Clim. Atmos. Sci.* **5** 16
Dee D P *et al* 2011 The ERA-interim reanalysis: configuration and performance of the data assimilation system *Q. J. R. Meteorol. Soc.* **137** 553–97
Dima I M and Wallace J M 2003 On the seasonality of the Hadley cell *J. Atmos. Sci.* **60** 1522–7
Dong D, Li J, Huyan L and Xue J 2017 Atmospheric energetics over the tropical Pacific during the ENSO cycle *J. Clim.* **30** 3635–54
Fang M and Tung K K 1999 Time-dependent nonlinear hadley circulation *J. Atmos. Sci.* **56** 1797–807
Fang X, Dijkstra H, Wieners C and Guardamagna F 2024 A nonlinear full-field conceptual model for ENSO diversity *J. Clim.* **37** 3759–74
Feng J, Ji X L, Li J P and He E Y 2023 Asymmetric impacts of El Niño development and decay stages on the Hadley circulation *Geophys. Res. Lett.* **50** e2023GL103861
Feng J, Li J P, An R and Wang Y Q 2021 Characteristics of the linkage between the boreal winter Hadley cell and various tropical sea surface temperature meridional structures *Int. J. Climatol.* **41** E463–E478
Feng J, Li J P, Jin F F, Liu Z Y, Nan X and Guo Y P 2016 Contrasting responses of the Hadley circulation to equatorially asymmetric and symmetric meridional sea surface temperature structures *J. Clim.* **29** 8949–63
Freitas A C V, Aímola L, Ambrizzi T and de Oliveira C P 2016 Changes in intensity of the regional Hadley cell in Indian Ocean and its impacts on surrounding regions *Meteorol. Atmos. Phys.* **129** 229–46
Gao C and Li G 2023 Decadal enhancement in the effect of El Niño in the decaying stage on the pre-flood season precipitation over Southern China *J. Clim.* **36** 8155–70
Gelaro R *et al* 2017 The modern-era retrospective analysis for research and applications, version 2 (MERRA-2) *J. Clim.* **30** 5419–54
Gill A E 2007 Some simple solutions for heat-induced tropical circulation *Q. J. R. Meteorol. Soc.* **106** 447–62
Guo Y P, Feng X B, Klingaman N P and Tan Z M 2020 Impact of Indo-Pacific warm pool Hadley circulation on the seasonal forecast performance for summer precipitation over the western North Pacific *Environ. Res. Lett.* **15** 104041
Guo Y P and Tan Z M 2018 Relationship between El Niño–Southern Oscillation and the symmetry of the Hadley circulation: role of the sea surface temperature annual cycle *J. Clim.* **31** 5319–32
Ham Y G, Lee H J, Jo H S, Lee S G, Cai W J and Rodrigues R R 2021 Inter-basin interaction between variability in the South Atlantic Ocean and the El Niño/Southern oscillation *Geophys. Res. Lett.* **48** e2021GL093338
Harrison D E and Chiodi A M 2015 Global seasonal precipitation anomalies robustly associated with El Niño and La Niña events—an OLR perspective*,+ *J. Clim.* **28** 6133–59
Hayashi M, Jin F F and Stuecker M F 2020 Dynamics for El Nino-La Nina asymmetry constrain equatorial-Pacific warming pattern *Nat. Commun.* **11** 4230
Held I M and Hou A Y 1980 Nonlinear axially symmetric circulations in a nearly inviscid atmosphere *J. Atmos. Sci.* **37** 515–33
Hersbach H *et al* 2020 The ERA5 global reanalysis *Q. J. R. Meteorol. Soc.* **146** 1999–2049
Hill S A, Bordoni S and Mitchell J L 2022 A theory for the Hadley cell descending and ascending edges throughout the annual cycle *J. Atmos. Sci.* **79** 2515–28
Hoskins B J and Yang G Y 2021 The detailed dynamics of the Hadley cell. Part II: December–February *J. Clim.* **34** 805–23
Hoskins B J, Yang G Y and Fonseca R M 2020 The detailed dynamics of the June–August hadley cell *Q. J. R. Meteorol. Soc.* **146** 557–75
Hou A Y 1998 Hadley circulation as a modulator of the extratropical climate *J. Atmos. Sci.* **55** 2437–57
Huang B *et al* 2017 Extended reconstructed sea surface temperature, version 5 (ERSSTv5): upgrades, validations, and intercomparisons *J. Clim.* **30** 8179–205
Hur I, Kim M J, Kwak K M, Sung H M, Byun Y H, Song H and Yoo C 2021 Hadley circulation in the present and future climate simulations of the K-ACE model *Asia-Pac. J. Atmos. Sci.* **58** 353–63

Jin F F 1997 An equatorial ocean recharge paradigm for ENSO. Part I: conceptual model *J. Atmos. Sci.* **54** 811–29
Kalnay E *et al* 1996 The NCEP/NCAR 40-year reanalysis project *Bull. Am. Meteorol. Soc.* **77** 437–71
Kanamitsu M, Ebisuzaki W, Woollen J, Yang S-K, Hnilo J J, Fiorino M and Potter G L 2002 NCEP–DOE AMIP-II reanalysis (R-2) *Bull. Am. Meteorol. Soc.* **83** 1631–44
Kim H-K and Lee S 2001 Hadley cell dynamics in a primitive equation model. Part I: axisymmetric flow *J. Atmos. Sci.* **58** 2845–58
Kim J W and Yu J Y 2022 Single- and multi-year ENSO events controlled by pantropical climate interactions *npj Clim. Atmos. Sci.* **5** 88
Kobayashi S *et al* 2015 The JRA-55 reanalysis: general specifications and basic characteristics *J. Meteorol. Soc. Japan* II **93** 5–48
Kohyama T and Tozuka T 2016 Seasonal variability of the relationship between SST and OLR in the Indian Ocean and its implications for initialization in a CGCM with SST nudging *J. Oceanogr.* **72** 327–37
Li Y, Du M Y, Feng J, Xu F L and Song W J 2023 Relationships between the Hadley circulation and tropical sea surface temperature with different meridional structures simulated in CMIP6 models *Front. Mar. Sci.* **10** 1145509
Liao H and Wang C 2021 Sea surface temperature anomalies in the Western Indian Ocean as a trigger for Atlantic Niño events *Geophys. Res. Lett.* **48** e2021GL092489
Liebmann B and Smith C A 1996 Description of a complete (interpolated) outgoing longwave radiation dataset *Bull. Am. Meteorol. Soc.* **77** 1275–7 (available at: www.jstor.org/stable/26233278)
Lindzen R S and Hou A V 1988 Hadley circulations for zonally averaged heating centered off the equator *J. Atmos. Sci.* **45** 2416–27
Lindzen R S and Nigam S 1987 On the role of sea surface temperature gradients in forcing low-level winds and convergence in the tropics *J. Atmos. Sci.* **44** 2418–36
Liu F, Zhang W, Jin F-F and Hu S 2021 Decadal modulation of the ENSO–Indian Ocean basin warming relationship during the decaying summer by the interdecadal pacific oscillation *J. Clim.* **34** 2685–99
Liu Y, Lu M, Yang H, Duan A, He B, Yang S and Wu G 2020 Land–atmosphere–ocean coupling associated with the Tibetan Plateau and its climate impacts *Natl Sci. Rev.* **7** 534–52
Ma J and Li J P 2008 The principal modes of variability of the boreal winter Hadley cell *Geophys. Res. Lett.* **35**
McCreary J P, Xie S P, Annamalai H and Murtugudde R 2005 Impact of Indian Ocean sea surface temperature on developing El Niño* *J. Clim.* **18** 302–19
Neelin J D, Battisti D S, Hirst A C, Jin F F, Wakata Y, Yamagata T and Zebiak S E 1998 ENSO theory *J. Geophys. Res.* **103** 14261–90
Nguyen H, Evans A, Lucas C, Smith I and Timbal B 2013 The Hadley circulation in reanalyses: climatology, variability, and change *J. Clim.* **26** 3357–76
Numaguti A 1995 Dynamics and energy balance of the Hadley circulation and the tropical precipitation zones. Part II: sensitivity to meridional SST distribution *J. Atmos. Sci.* **52** 1128–41
Piao J, Chen W, Chen S, Gong H, Chen X and Liu B 2020 The intensified impact of El Niño on late-summer precipitation over East Asia since the early 1990s *Clim. Dyn.* **54** 4793–809
Rayner N A, Parker D E, Horton E B, Folland C K, Alexander L V, Rowell D P, Kent E C and Kaplan A 2003 Global analyses of sea surface temperature, sea ice, and night marine air temperature since the late nineteenth century *J. Geophys. Res.* **108**
Song F and Zhou T 2015 The crucial role of internal variability in modulating the decadal variation of the east Asian summer monsoon–ENSO relationship during the Twentieth Century *J. Clim.* **28** 7093–107
Song X M, Zhang R H and Rong X Y 2019 Influence of intraseasonal oscillation on the asymmetric decays of El Niño and La Niña *Adv. Atmos. Sci.* **36** 779–92
Song X M, Zhang R H and Rong X Y 2022 Dynamic causes of ENSO decay and its asymmetry *J. Clim.* **35** 445–62
Soulard N, Lin H and Yu B 2019 The changing relationship between ENSO and its extratropical response patterns *Sci. Rep.* **9** 6507
Stechmann S N and Ogrosky H R 2014 The walker circulation, diabatic heating, and outgoing longwave radiation *Geophys. Res. Lett.* **41** 9097–105
Stuecker M F, Jin F F and Timmermann A 2015 El Niño−Southern oscillation frequency cascade *Proc. Natl Acad. Sci.* **112** 13490–5
Sun Y, Li L Z X, Ramstein G, Zhou T, Tan N, Kageyama M and Wang S Y 2019 Regional meridional cells governing the interannual variability of the Hadley circulation in boreal winter *Clim. Dyn.* **52** 831–53
Sun Y and Zhou T J 2014 How does El Niño affect the interannual variability of the boreal summer Hadley circulation? *J. Clim.* **27** 2622–42
Timmermann A *et al* 2018 El Nino-Southern oscillation complexity *Nature* **559** 535–45
Wang B *et al* 2023 Understanding the recent increase in multiyear La Niñas *Nat. Clim. Change* **13** 1075–81
Wang B, Wu R G and Fu X H 2000 Pacific–East Asian teleconnection: how does ENSO affect East Asian climate? *J. Clim.* **13** 1517–36
Wang C 2019 Three-ocean interactions and climate variability: a review and perspective *Clim. Dyn.* **53** 5119–36
Wang J-Z and Wang C 2021 Joint boost to super El Niño from the Indian and Atlantic Oceans *J. Clim.* **34** 4937–54
Wang Y, Feng J, Li J, An R and Wang L 2019 Variability of boreal spring Hadley circulation over the Asian monsoon domain and its relationship with tropical SST *Clim. Dyn.* **54** 1655–69
Wang Y, Hu K, Huang G and Tao W 2021 Asymmetric impacts of El Niño and La Niña on the Pacific–North American teleconnection pattern: the role of subtropical jet stream *Environ. Res. Lett.* **16** 114040
Weisberg R H and Wang C Z 1997 A Western Pacific oscillator paradigm for the El Niño-Southern oscillation *Geophys. Res. Lett.* **24** 779–82
Xie X R, Huang P, Zhou S J and Zhang J Y 2022 Changes in ENSO-driven Hadley circulation variability under global warming *Atmos. Res.* **274** 106220
Xu W 2013 Precipitation and convective characteristics of summer deep convection over East Asia observed by TRMM *Mon. Weather Rev.* **141** 1577–92
Yang X K and Huang P 2021 Restored relationship between ENSO and Indian summer monsoon rainfall around 1999/2000 *Innovation* **2** 100102
Yu M X, Feng J, Li J P and An R 2022 Interdecadal shift of the El Niño's modulation on the connection between the Hadley circulation and tropical SST *Clim. Dyn.* **60** 2167–81
Yun K-S, Timmermann A and Stuecker M F 2021 Synchronized spatial shifts of Hadley and walker circulations *Earth Syst. Dyn.* **12** 121–32
Zaplotnik Ž, Pikovnik M and Boljka L 2022 Recent Hadley circulation strengthening: a trend or multidecadal variability? *J. Clim.* **35** 4157–76
Zhang K, Randel W J and Fu R 2016 Relationships between outgoing longwave radiation and diabatic heating in reanalyses *Clim. Dyn.* **49** 2911–29
Zhou B T and Wang H J 2006 Interannual and interdecadal variations of the hadley circulation and its connection with tropical sea surface temperature *Chin. J. Geophys.* **49** 1147–54
Zhou C, Lu J, Hu Y Y and Zelinka M D 2020 Responses of the Hadley circulation to regional sea surface temperature changes *J. Clim.* **33** 429–41
Zurita-Gotor P 2019 The role of the divergent circulation for large-scale eddy momentum transport in the tropics. Part I: observations *J. Atmos. Sci.* **76** 1125–44